Composites Part B 272 (2024) 111098

Contents lists available at ScienceDirect

Composites Part B

journal homepage: www.elsevier.com/locate/composites

A novel methodology to measure the transverse Poisson's ratio in the elastic and plastic regions for composite materials

I.R. Cózar [a,*], J.J. Arbeláez-Toro [a,b], P. Maimí [a], F. Otero [c,d], E.V. González [a], A. Turon [a], P.P. Camanho [e,f]

[a] AMADE, Polytechnic School, University of Girona, Campus Montilivi s/n, 17071 Girona, Spain
[b] Faculty of Engineering, Instituto Tecnológico Metropolitano, Medellín, Colombia
[c] CIMNE, Universitat de Politècnica de Catalunya, 08034 Barcelona, Spain
[d] Department of Nautical Science and Engineering, Universitat Politècnica de Catalunya, Pla de Palau 18, 08003 Barcelona, Spain
[e] DEMec, Faculdade de Engenharia, Universidade do Porto, 4200-465 Porto, Portugal
[f] INEGI, Instituto de Ciência e Inovação em Engenharia Mecânica e Industrial, 4200-465 Porto, Portugal

ARTICLE INFO

Keywords:
Mechanical properties
Thermoplastic resin
Carbon fibre
Plastic deformation
Mechanical testing

ABSTRACT

A new methodology to measure the transverse Poisson's ratios in fibre-reinforced composite materials was developed. Transverse tensile and transverse compressive standardised tests were instrumented using digital image correlation equipment to measure the lateral strain field of the specimens. A thermoplastic-based composite material was used to describe the proposed methodology. The elastic transverse Poisson's ratio exhibits a different behaviour in tension than in compression, its value being greater in compression than in tension. Assuming no plastic strain in the longitudinal direction, the plastic transverse Poisson's ratio in compression suggests no volumetric plastic strains for small axial plastic strains, however, plastic dilatancy was observed when the amount of compressive plastic axial strain increases.

1. Introduction

Unidirectional fibre-reinforced polymer (FRP) composite materials behave as homogenous transversely isotropic materials [1–4] and, thus, have a plane of symmetry with respect to a rotation about the fibre-oriented axis. The material properties of this transverse plane are the same in all directions. Therefore, five elastic material properties are required in the generalised Hooke's law. Several standardised methodologies have been developed to measure them: the longitudinal Young's modulus [5,6], the transverse Young's modulus [5,6], the shear Young's modulus [7–9], and the elastic longitudinal Poisson's ratio (ν_{12}, where subindex 1 refers to the fibre dominant direction and subindex 2 to the in-plane matrix dominant direction) [5]. However, there is no standardised method for measuring the elastic transverse Poisson's ratio (ν_{23}, where subindex 3 refers to the through-the-thickness matrix dominant direction).

FRP composite materials exhibit nonlinear response under certain loading conditions, such as compressive or shear loading states in the directions governed by the matrix. This behaviour is largely due to plastic strains, especially in thermoplastic-based composite materials [10,11]. The evolution of the plastic strains is governed by the plastic transverse Poisson's ratio (ν_{23}^{p}). Several constitutive models, developed to predict the inelastic deformation due to plastic strains, use a non-associative plastic flow rule and they can be adjusted using ν_{23}^{p} [12–16].

In solid mechanics, ν_{23} is defined as the negative quotient of the transverse strain (ε_{33}) to the axial strain applied (ε_{22}) on the transverse plane. Transverse Poisson's ratio is an important material property of FRPs in the elastic and plastic regions. In the literature, few works are addressed to the experimental measurement of ν_{23}. Recently, Khaled et al. [17] carried out a transverse tensile and compressive tests using a unidirectional carbon/epoxy composite material. Specimens with fibres aligned through-the-thickness of the panel were employed, thus limiting the width and length of the specimens to the thickness of the panel. The authors used 96 plies per panel which equals to 18.3 mm specimen length. Curing thick laminates can lead to significant residual stresses which can cause delamination cracking and residual shape distortions [18–20]. Furthermore, special gripping assemblies were manufactured to transfer the load from a hydraulic grip onto the specimen. The strain fields were measured with digital image correlation (DIC) techniques. The elastic Poisson's ratio from tensile tests was reported, and the elastic and plastic Poisson's ratios from compressive tests were also presented.

* Corresponding author.
E-mail address: ivan.ruiz@udg.edu (I.R. Cózar).

https://doi.org/10.1016/j.compositesb.2023.111098
Received 16 June 2023; Received in revised form 25 October 2023; Accepted 5 November 2023
Available online 18 December 2023

Frederiksen [21] presented an approach to estimate ν_{23} of unidirectional FRP laminates from the natural frequencies of a plate specimen. The measurement of frequencies was obtained through non-destructive impact testing and a model analysis, and ν_{23} was estimated based on the higher-order shear deformation theory [22] and an optimisation algorithm. Kohlhauser and Hellmich [23] proposed a methodology to estimate the elastic material constants of isotropic, transversely isotropic and orthotropic materials by combining ultrasonic-mechanical and uniaxial tests. The method is based on the generalised Hooke's law, the authors presented an approach to estimate the components of the stiffness tensor using an ultrasonic-mechanical test. The material properties of a carbon/aluminium composite material were estimated. First, the Young's modules were obtained from uniaxial tests. Subsequently, several ultrasonic pulse transmission tests were performed at different directions and the components of the stiffness tensor were calculated. Finally, the Poisson's ratios were estimated from the stiffness tensor. The only use of ultrasonic-mechanical testing leads to significant errors in the estimation of ν_{23}. Kohlhauser and Hellmich [23] reported a relative error between the measured ν_{23} from ultrasonic-mechanical tests and the one estimated by the combined method higher than 70% in FRPs. Accordingly, the estimation of ν_{23} based on the modal analyses or ultrasonic-mechanical techniques is a current challenge [24].

De Baere et al. [25] carried out tensile tests to measure the longitudinal Poisson's ratio (ν_{12}) from a wave cross-ply laminate using a carbon fibre thermoplastic-based composite material. The experimental data showed a clear tendency for ν_{12} to decrease when the longitudinal strain exceeds 0.6%. The authors analysed the influence of the experimental methodology on this tendency. Different tensile loading levels and cycle tests were employed, with different measuring equipment (strain gauges, optical fibre and extensometer). The authors concluded that the relationship between ν_{12} and longitudinal strain, as observed in the experimental data, reflects the material's behaviour rather than any influence from the experimental setup. Yilmaz et al. [26] also analysed the relationship between ν_{12} and the longitudinal strain of different stacking sequences of a glass fibre thermoset-based composite material (stitched fabric technology). Similar experimental setups to those conducted in [25] were employed. The authors concluded that the ν_{12} decreases as the longitudinal strain increases because the transverse microcracks release the compressive strain in the transverse direction.

Alternatively, micromechanical finite element (FE) models can also be employed to estimate ν_{23}. Generally, several loading states are applied to micromechanical FE models using characterised constituent materials (fibre and matrix). Then, the Hooke's law and the averaging techniques [27] are applied to the numerical results and the meso elastic material properties can be determined [28,29]. In addition, micromechanical-based analytical models are used to estimate ν_{23} [30]. Furthermore, out-of-plane material properties can be estimated using inverse identification methods combining experimental data and FE models. Seon et al. [31] carried out an open-hole compressive test using a carbon/epoxy material and DIC equipment to measure the surface strain field. The authors employed an algorithm to minimise the least square error between the DIC-measured strain field and FE models-predicted strains by tuning the elastic material properties of the FE model.

In many works in the literature, the value of the transverse Poisson's ratios is assumed [13,15,32,33], as well as the transverse shear modulus [34]. There is no standardised test to experimentally measure the elastic and plastic values of transverse Poisson's ratios. In the present work, a new methodology is proposed to measure the elastic transverse Poisson's ratio in tension (ν_{23T}) and in compression (ν_{23C}) as well as the plastic transverse Poisson's ratio in compression (ν^{p}_{23C}) from standardised tests for measuring elastic and strength properties [5,6]. The methodology and data reduction approach is described in Section 2. The measured transverse Poisson's ratios are discussed in Section 3. Finally, the main conclusions of this work are presented.

2. Methodology

2.1. Material and methods

The analysed material was a carbon fibre-reinforced poly-ether-ether-ketone (PEEK). The consolidated ply thickness of a unidirectional laminate was equal to 0.182 mm and a fibre volume content of 56%. The hot stamping manufacturing process was employed following the manufacturing procedure from the material supplier. All panels were examined through an ultrasound non-destructive inspection using a C-scan technique to ensure good consolidation of the laminates.

The total strain field of each specimen was measured using both strain gauges and DIC equipment. Then, the total strain was decomposed into two components: elastic strain and plastic strain. At the beginning of each test, the total strain was deemed to be elastic strain until the stress–strain relationship was not linear (see Fig. 6). Subsequently, unloaded–reloaded steps were performed in which the external load vanishing, thus the total strain was considered as plastic strain.

2.2. Transverse tensile test

The elastic transverse Poisson's ratio in tension (ν_{23T}) was measured from a transverse tensile test. However, the plastic Poisson's ratio in tension could not be obtained from this test since no plastic strains were found. The test was carried out following the ASTM-D3039M standard [5] and using DIC equipment. Three specimens with 25 mm × 175 mm in-plane dimensions with a stacking sequence of $[90]_{11}$ were tested. Glass fibre tabs 25 mm long were used at the ends of the specimens to prevent slippage between the tester clamps and the specimens, ensuring a uniform stress field around the clamping tool. The thickness and dimensions of the specimens were verified and accomplished the ASTM-D3039M standard. Therefore, the dimensions and shape of the specimens ensure a uniform strain field along their gauge length.

An electromechanical testing machine MTS Insight50 with a 50 kN capacity using manual grips was employed for the transverse tensile test, see Fig. 1.a. In addition, a 50 kN MTS load cell calibrated at 100% was used. The tensile test was conducted under displacement control at 2 mm/min at room temperature.

The DIC equipment was located on the lateral surface of the specimens to measure the total axial strain ($\bar{\varepsilon}^{DIC}_{22}$) (the in-plane direction perpendicular to the fibre dominant direction) and the total out-of-plane strain ($\bar{\varepsilon}^{DIC}_{33}$), see Fig. 2.a. In addition, two strain gauges located on the in-plane surfaces of the specimens (one on the top face and the other on the bottom face, see Fig. 2.a) and aligned with the load direction were used. The measurements from the strain gauges were employed to cross-validate the measurement of ε_{22} from the DIC equipment. The specimens were loaded until their failure was reached (see Fig. 2.c), and the load, the gauge strains and the DIC displacement fields were stored during the test.

2.3. Transverse compressive test

The elastic transverse Poisson's ratio in compression (ν_{23C}), as well as in the plastic region (ν^{p}_{23C}), from a transverse compressive test were measured. The in-plane dimensions of the specimens were 13 mm × 140 mm, following the ASTM-6641M standard [6]. Three specimens with a stacking sequence of $[90]_{22}$ were tested. Glass fibre tabs 64 mm long and located on the ends of the specimens to avoid the slippage between the tester clamps and the specimens were added. The dimensions of the specimens meet the requirements of the ASTM-6641M standard. Consequently, the dimensions and shape of the specimens ensure a uniform strain field along their gauge length.

A servo-hydraulic test machine MTS Insight300 with a capacity of 300 kN and an MTS 300 kN load cell calibrated at 100% were used. In

Fig. 1. Experimental setup of the transverse tensile (a) and compressive (b) tests.

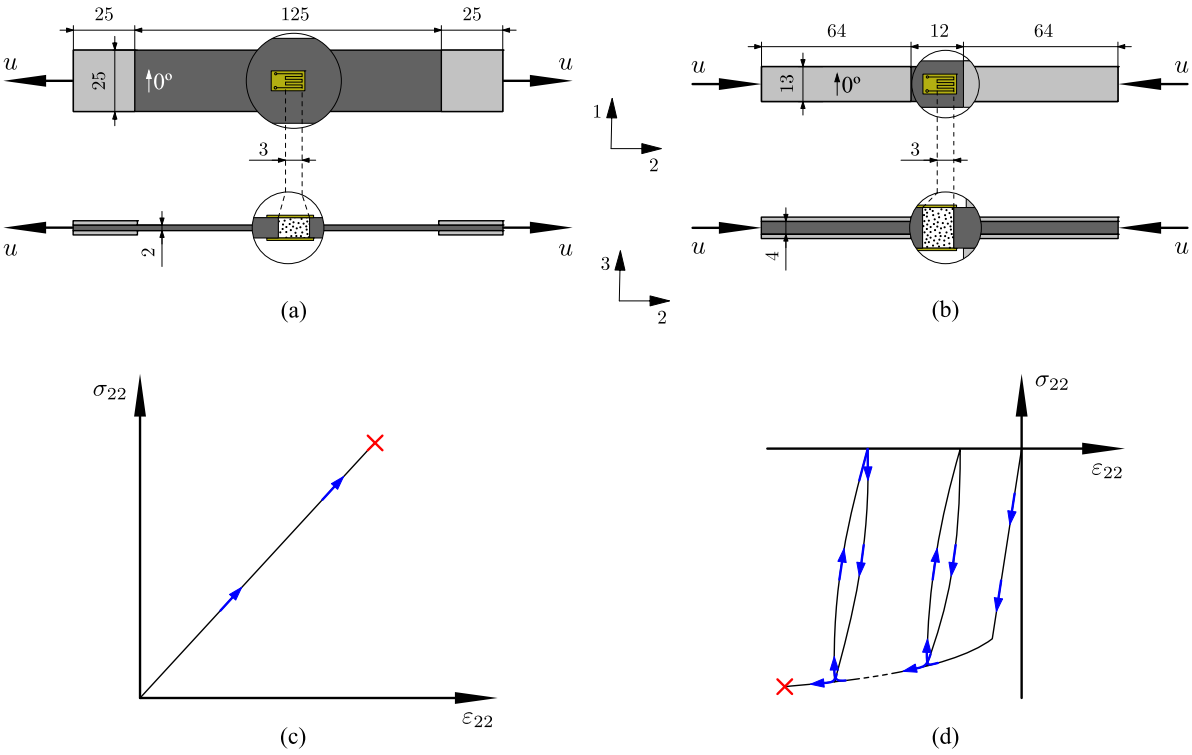

Fig. 2. Schematic representation of: (a) and (c) transverse tensile test, and (b) and (d) transverse compressive test. 1 refers to the longitudinal direction, and 2 and 3 to the transverse directions. All dimensions are in mm.

addition, the compressive plates and the fixture system from the ASTM-D6641M standard [6] were employed, see Fig. 1.b. The compressive test was carried out under displacement control at 2 mm/min at room temperature.

As with the tensile test, DIC equipment was located on the lateral surface of the specimens to measure the total axial and out-of-plane strains, see Fig. 2.b. The axial strain was also measured using two strain gauges (one on the top face and the other on the bottom face, see Fig. 2.b) to cross-validate the measurement of ε_{22} from the DIC equipment but also to quantify the percent bending.

In this test, the specimens were loaded under transverse compression until to the onset of the plastic region (when the linearity in the axial stress (σ_{22}) vs. axial strain curve was lost) and, then the specimens were unloaded. After that, the specimens were reloaded to increase the plastic strains (ε^p_{22} and ε^p_{33}, axial and out-of-plane plastic strains, respectively) and, then were unloaded. This last cycle was repeated until the specimens failed, see Fig. 2.d. The load in the unloaded steps was not equal to zero. A residual load (aprox. 2% of the peak load of the first cycle) was used to prevent readjustment and movements between the specimen clamping tool and the test machine. Otherwise, the DIC measurements can be affected since the relative position between the specimen and the DIC equipment can change. This residual load produces an error relative less than 0.9% in the transverse Poisson's ratios compared to releasing the specimens. Furthermore, the effect of the residual load can be seen in Fig. 11.a where $\sigma_{22} \approx 0$ at the end of each unloading cycle. In addition, the residual load was held for 15 s, which corresponds to 75 DIC images, to avoid viscous effects due to dynamic loading conditions, see Fig. 3. No significant relaxation of the material was observed when the specimens were in the unloaded steps under the residual load. Therefore, 15 s is a conservative value.

2.4. Instrumentation and data reduction

The data acquisition system used in this work can be divided into two main groups: a QuantumX system to measure the load and the axial strain from strain gauges, and a 2D DIC acquisition system to measure the axial and through-the-thickness strains. The strain gauges used were HBM LY41-3/350. The DIC equipment was composed of a 5 megapixels

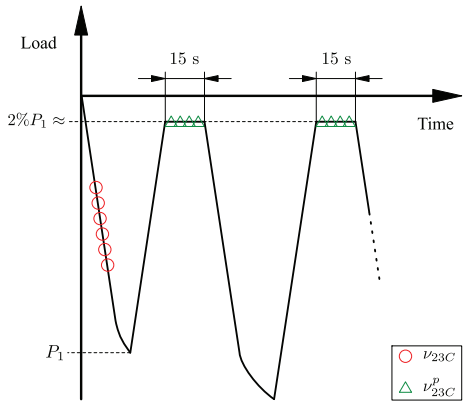

Fig. 3. Schematic representation of load vs. time curve of the transverse compressive test. The elastic transverse Poisson's ratio was measured where the red circles are located, and the plastic transverse Poisson's ratio was measured where the green triangles are located.

camera with a 2/3 in. CCD sensor providing 14-bit grayscale images. The lens was selected from the MachVis software for a field of view of 10 mm, resulting in a focal length of 120 mm and two extension tubes of 24 mm and 12 mm. The lens aperture size was set equal to f/11 to avoid lens distortions or diffraction limits [35]. The exposure time was fixed to 8 ms, less than the inverse of the focal length [36]. The Vic2D commercial software was used to post-process the data from the DIC equipment with a subset of 77 and a step of 17. Different values of the subset and step were tested and no significant differences were found in the analysed data.

The analysed area of the DIC equipment was similar to the measuring grid of the strain gauges (3 mm × 2.5 mm). The measured strain from a strain gauge is the average value of the strains under its measuring grid [37]. Furthermore, the DIC equipment was centered with respect to the strain gauges, see Fig. 2.a and b. Therefore, the average values of the DIC axial strain field were compared with the measurements of the strain gauges. The average strain from the DIC equipment was calculated as

$$\bar{\varepsilon}^{DIC}_{ij} = \frac{1}{A_{DIC}} \int_A \varepsilon^{DIC}_{ij} d\Omega_{DIC} \tag{1}$$

where A_{DIC} is the DIC area analysed, Ω_{DIC} refers to the DIC area domain, ε^{DIC}_{ij} is the strain field in the ij direction in the Cartesian coordinate system.

The relative error of the DIC axial strain with respect to the average strain obtained from the two strain gauges was calculated. This relative error in the elastic region was used to test the reliability of the present methodology. In the present work, DIC strain refers to the average value of the strain field obtained from the DIC equipment for the corresponding loading state ($\bar{\varepsilon}^{DIC}_{ij}$).

The elastic transverse Poisson's ratios for both tensile and compressive tests were calculated as

$$\nu_{23} = -\frac{\varepsilon^e_{33}}{\varepsilon^e_{22}}. \tag{2}$$

where ε^e_{22} and ε^e_{33} are the axial and out-of-plane elastic strains, respectively. Both strains were obtained from the DIC equipment and the ratio was calculated. The elastic strains in the compressive test were captured in the first cycle of the σ_{22} vs. ε_{22} curves at the straight part (red circles in Fig. 3).

The plastic transverse Poisson's ratio under compression was calculated as

$$\nu^p_{23C} = -\frac{\varepsilon^p_{33}}{\varepsilon^p_{22}}. \tag{3}$$

Both plastic strains were obtained from the compressive test in the unloaded steps. DIC strains measured at these unloaded steps were assumed to be plastic strains and used in Eq. (3). Therefore, several ν^p_{23C} at each plastic axial strain were measured (green triangles in Fig. 3).

The proposed methodology is summarised in Fig. 4 for the transverse compressive test. The specimen was loaded under transverse compressive loading stress state before reaching the non-linear relationship in the σ_{22} vs. ε_{22} curve. The strain field of the lateral surface of the specimen was then calculated from the displacement field measured by the DIC equipment. Subsequently, the average of the strain field was calculated with Eq. (1) and they were assumed to be elastic strains. Finally, the elastic transverse Poisson's ratio in compression was calculated from Eq. (2) and graphical represented as a function of ε^e_{22}, see Fig. 4.a. Similar procedure was used for ν^p_{23C} when the specimen was unloaded after non-linear σ_{22}-ε_{22} relationship was observed, see Fig. 4.b. In this case, the DIC strain was assumed to be the plastic strain when no external load was applied. The last cycle was repeated several times.

Once the tests were finished, the transverse Poisson's ratios were also obtained by performing a linear regression analysis of the corresponding axial strain vs. out-of-plane strain curves. The absolute value of the slopes of the linear regression analyses from each analysis was considered as the corresponding transverse Poisson's ratio. The intercept of the corresponding linear regression was forced equal to zero, since no out-of-plane strain is expected when no axial strain is applied.

The random error of the measured strains from the strain gauges was calculated as

$$\mathbb{E}_{SG} = \pm \Delta \mathbb{E}_{SG}, \tag{4}$$

where $\Delta\mathbb{E}_{SG}$ is the accuracy from the data acquisition system plus that of the strain gauges. This accuracy was obtained through a calibration certificate from an external laboratory.

The source of uncertainty for the DIC strain measurements in the elastic region can be divided into two main groups: random error ($\mathbb{E}_{rand}$) and standard error ($\mathbb{E}_{std}$). The random error may come from the DIC equipment, the speckle pattern, the lighting, environmental influences, the correlation algorithm [38–40], etc, whereas the standard error is related to the standard deviation of the corresponding strain field ($S_{\bar{\varepsilon}^{DIC}_{ij}}$) in each interval time (DIC image).

The random error from the DIC equipment was quantified as

$$\mathbb{E}_{rand_{ij}} = \pm \Delta \mathbb{E}_{rand_{ij}}, \tag{5}$$

where $\Delta\mathbb{E}_{rand}$ is the noise-floor of the DIC measurements. $\Delta\mathbb{E}_{rand_{ij}}$ was estimated for each specimen at the beginning of each test by acquiring the DIC strains over a time period (aprox. 10 s, 50 DIC images) when the specimen was unloaded [41,42]. Therefore, zero strains should be measured in this step since zero displacements were applied. However, all measured DIC strains must result from random error. Consequently, the average value of each DIC strain during this time period was considered to be $2\Delta\mathbb{E}_{rand_{ij}}$ for each direction ($\Delta\mathbb{E}_{rand_{22}}$ for $\bar{\varepsilon}^{DIC}_{22}$ and $\Delta\mathbb{E}_{rand_{33}}$ for $\bar{\varepsilon}^{DIC}_{33}$).

The standard error of the DIC strains in the elastic region was estimated as

$$\mathbb{E}_{std_{ij}} = \pm z_{\alpha/2} \frac{S_{\bar{\varepsilon}^{DIC}_{ij}}}{\sqrt{N_{px}}}, \tag{6}$$

where $z_{\alpha/2}$ is the confidence range, and N_{px} refers to the number of pixels of each analysed area with the DIC equipment. A normal distribution of the samples and a level of confidence equal to 95% were assumed ($z_{\alpha/2} = 1.960$). Finally, the Euclidean norm of $\mathbb{E}_{rand_{ij}}$ and $\mathbb{E}_{std_{ij}}$ was proposed to determine the uncertainty of each measured DIC strain in the elastic region,

$$\mathbb{E}_{DIC_{ij}} = \sqrt{\mathbb{E}^2_{rand_{ij}} + \mathbb{E}^2_{std_{ij}}}. \tag{7}$$

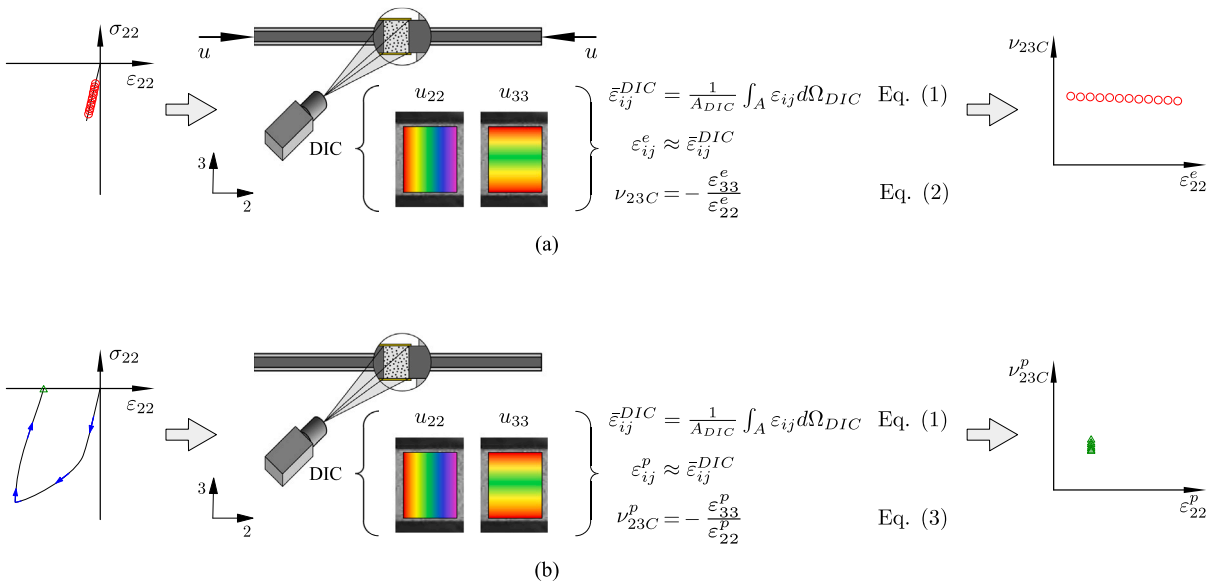

Fig. 4. Schematic representation of the procedure to measure the elastic (a) and plastic (b) transverse Poisson's ratios in compression.

Table 1
Accuracy of the equipment used in the experimental tests, the different rows represent different specimens.

Measurement instrument			Test	
			Tensile	Compressive
Strain gauges	$\Delta\mathbb{E}_{SG}$	($\mu\varepsilon$)	0.28	
DIC	$\Delta\mathbb{E}_{rand_{22}}$	($\mu\varepsilon$)	13.26	24.07
			5.89	4.05
			6.79	55.90
	$\Delta\mathbb{E}_{rand_{33}}$	($\mu\varepsilon$)	33.65	1.94
			19.56	2.78
			7.75	21.53

The uncertainty of the elastic transverse Poisson's ratios (ν_{23T} and ν_{23C}) from the DIC equipment was estimated as

$$\mathbb{E}_{\nu_{23}} = \left|\frac{\partial \nu_{23}}{\partial \varepsilon_{22}^{e}}\right| \Delta\mathbb{E}_{rand_{22}} + \left|\frac{\partial \nu_{23}}{\partial \varepsilon_{33}^{e}}\right| \Delta\mathbb{E}_{rand_{33}}, \tag{8}$$

where ε_{22}^{e} and ε_{33}^{e} were measured from the tensile test for the uncertainty of ν_{23T} in $\mathbb{E}_{\nu_{23T}}$, or from the compressive test for the uncertainty of ν_{23C} in $\mathbb{E}_{\nu_{23C}}$. The uncertainty of ε_{22}^{p} was estimated using Eq. (7), where the same noise-floors in Eq. (5) were used. Moreover, the uncertainty of ν_{23}^{p} was also quantified using Eq. (8) replacing the elastic strains by the plastic strains.

3. Results and discussion

The accuracy of the strain gauges and the noise-floor of the DIC equipment from each test are summarised in Table 1. The accuracy of the strain gauges is better than that of the DIC equipment. Moreover, there is no clear trend in the DIC accuracy according to the test nor to the strain direction. As will be shown later, the accuracy of the equipments were suitable for the measurements carried out in the present work. Three specimens per each test were used, hence, the rows in the tables and the symbols in the figures represent the results from each specimen tested. The error bars displayed in the figures correspond to the errors explained in Section 2.4 and the no significant errors were omitted for the sake of clarity.

Uniform lateral strain fields were observed during the tensile test, see the strain field of ε_{22}^{DIC} and ε_{33}^{DIC} at the same external load ($\bar{\varepsilon}_{22}^{DIC} \approx$ 0.5%) in Fig. 5.a. However, non-uniform strain fields were measured from the compressive test (see Fig. 5.b) evidencing that the specimens were undergoing some bending. This misalignment may come from imperfections in the specimens, the test fixture, the testing procedure, etc. Nonetheless, the percent bending for each specimen met the requirements of the ASTM-6641M standard (they were less than 9.3% < 10%). Furthermore, the observed failure modes in the compressive test accomplished the standard.

The elastic axial strain (ε_{22}^{e}) was captured from 3000 μm/m to 7500 μm/m of the total strain, see Fig. 6. The values of σ_{22} in Fig. 6 have been omitted since the material supplier has proprietary of the data. Within this range, there was enough strain to be properly measured. In the present work, the relative error of the DIC equipment with respect to the strain gauges significantly increases for ε_{22}^{e} less than 3000 μm/m (relative error greater than 12.5%). Furthermore, the relative error of the slope from the σ_{22} vs. ε_{22} curve (obtained from the cross-head load cell and the strain gauges, respectively) with respect to the transverse Young's modulus (provided by the material supplier) was less than 6.1% in tension and 0.5% in compression. Therefore, axial strain within 3000 μm/m and 7500 μm/m in absolute terms can be assumed to be an elastic strain in both loading states (tension and compression) for the selected material (no plastic strains were considered within this range).

As explained in Section 2, the DIC axial strain was compared with the average strain measured from two strain gauges located on the in-plane surfaces of the specimens. The comparison demonstrated the ability of the DIC setup to capture the axial strain in the transverse tensile test, see Fig. 7. The DIC axial strain measured from two of the three specimens was greater than that measured from the strain gauges; being greater when ε_{22}^{e} increases. However, the DIC axial strain from the third specimen was under the gauge measurements; being smaller when ε_{22}^{e} decreases. The relative error of ε_{22}^{e} for each specimen was calculated, and the highest relative error was less than 12.5%.

A clear trend of ν_{23T}, obtained from Eq. (2), as a function of ε_{22}^{e} was found in the transverse tensile test, see Fig. 8. The transverse Poisson's ratio in tension (ν_{23T}) decreases when elastic axial strain (ε_{22}^{e}) increases for two of the three specimens tested. A linear regression analysis using ν_{23T} as a function of ε_{22}^{e} from all three specimens was performed. The obtained slope (−0.10) of this regression analysis confirms the trend, but it is also noteworthy that a coefficient of variation of ν_{23T} less than 7.9% was observed. This behaviour was also observed in the ν_{12}-longitudinal strain relationship of glass FRP laminates [25,26]. Yilmaz et al. [26] attributed the reduction of ν_{12} when the longitudinal strain

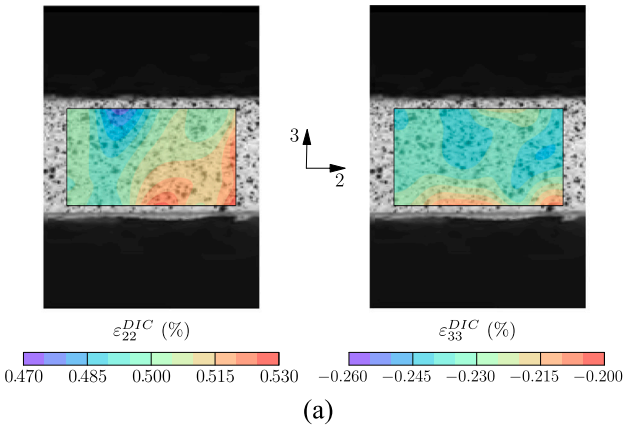

Fig. 5. Lateral strain field from the transverse tensile (a) and compressive (b) tests using the DIC equipment at abs(ε_{22}^{DIC}) ≈ 0.5%. The specimens were loaded in the horizontal direction (2-axis direction).

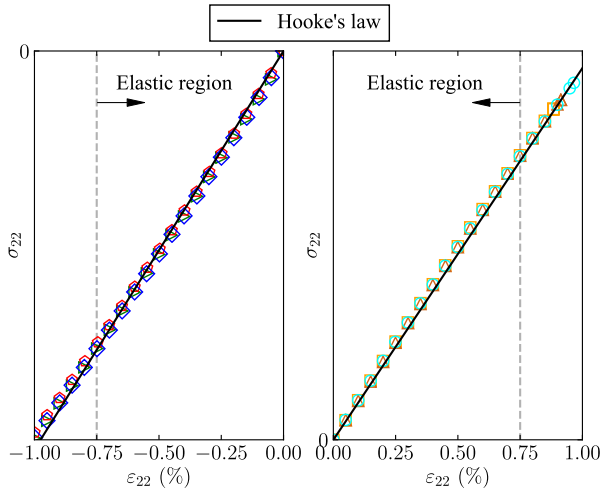

Fig. 6. Stress vs. strain curve obtained from the transverse compressive (left) and tensile (right) tests using the average strain from the two strain gauges, the different marks represents different specimens. For the sake of clarity, the error bars are omitted since no significant error was measured.

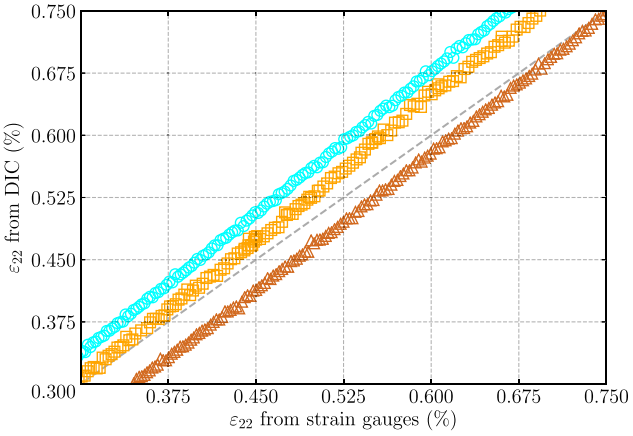

Fig. 7. Goodness-of-fit plot of the DIC axial strain vs. average strain measured from the two strain gauges from the transverse tensile test, the different marks represents different specimens. For the sake of clarity, a dashed straight curve with slope equal to 1 is shown and the error bars are omitted since no significant error was measured.

increases due to transverse microcracking. In addition, the coefficient of determination ($R^2 = 1.00$) indicates that ν_{23T} is linearly proportional to ε_{22}^e in the analysed range of ε_{22}^e. The measured errors of ν_{23T} and ε_{22}^e were not significant since the biggest error of ν_{23T} was $\mathbb{E}_{\nu_{23T}} = 5.06 \times 10^{-3}$ and that of ε_{22}^e was $\mathbb{E}_{DIC_{22}} = 34.43 \times 10^{-4}$%.

The DIC axial strain measured from the transverse compressive test was also compared with the average strain from the strain gauges in Fig. 9. In all the specimens, the DIC axial strain was higher vs. the strain measured using the strain gauges; being smaller when the amount of the compressive ε_{22}^e increases. The highest relative error was less than 6.2%. Therefore, the DIC equipment also properly measured ε_{22} in the transverse compressive test.

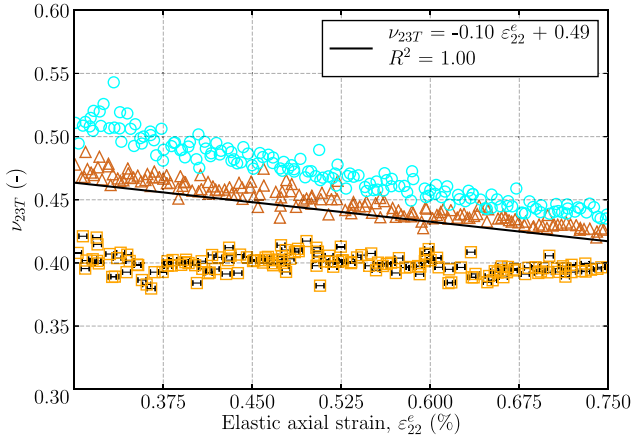

Fig. 8. Elastic transverse Poisson's ratio in tension vs. DIC elastic axial strain, the different marks represents different specimens.

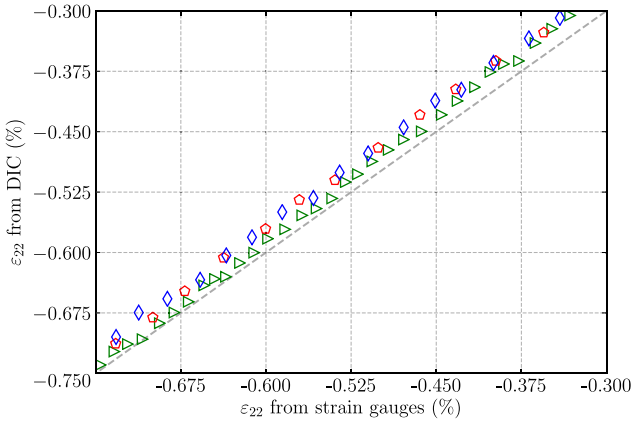

Fig. 9. Goodness-of-fit plot of the DIC axial strain vs. average strain measured from the strain gauges from the transverse compressive test, the different marks represents different specimens. For the sake of clarity, a dashed straight curve with slope equal to 1 is shown and the error bars are omitted since no significant error was measured.

As for ν_{23T}, a similar trend is obtained from the measured ν_{23C} using Eq. (2) in all three specimens, see Fig. 10. The transverse Poisson's ratio measured in compression (ν_{23C}) decreases when the amount of compressive elastic axial strain (ε^e_{22}) increases. In addition, a linear regression analysis was also carried out of ν_{23C} vs. ε^e_{22} using the measured values from all three specimens. The slope (0.11) of this regression analysis confirms this trend, but it is also noteworthy that a coefficient of variation of ν_{23C} less than 4.3% was observed. Furthermore, the coefficient of determination (R^2 = 1.00) also indicates that ν_{23C} is linearly proportional to ε^e_{22} in the analysed range of ε^e_{22}. Again, the measured errors of ν_{23C} and ε^e_{22} were not significant since the biggest error of ν_{23C} was $\mathbb{E}_{\nu_{23C}} = 2.30 \times 10^{-2}$ and that of ε^e_{22} was $\mathbb{E}_{DIC_{22}} = 26.26 \times 10^{-4}$%. It is worth mentioning that the elastic transverse Poisson's ratio does not follow a linear dependency of the axial strain when $\varepsilon^e_{22} = (-0.3, 0.3)$%, since the intercepts of Figs. 8 and 10 are different.

The elastic Poisson's ratio in compression (ν_{23C}) was also measured from the rest of the cycles performed in the transverse compressive tests, the results of Figs. 9 and 10 correspond to the elastic region of the first cycle under loading conditions. The elastic transverse strains (ε^e_{22} and ε^e_{33}) of the remaining cycles were estimated by subtracting the corresponding plastic strains from the total strains measured by the DIC equipment under equal stress level, see Fig. 11.a where the zoom corresponds to the referenced stress range. No significant differences

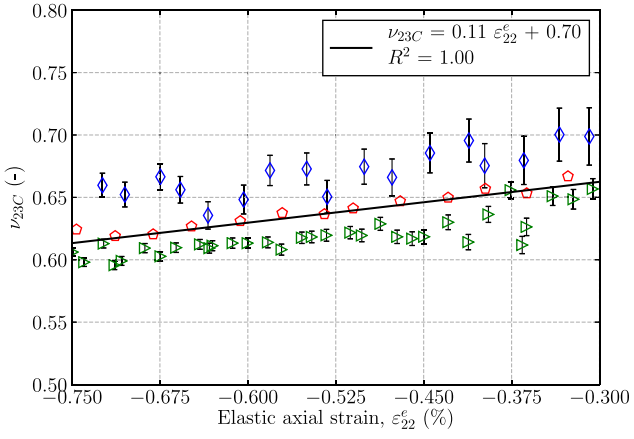

Fig. 10. Elastic transverse Poisson's ratio in compression vs. DIC elastic axial strain, the different marks represents different specimens.

were observed in ν_{23C} between the different cycles before to plastic strains, see Fig. 11.b from the first cycle to the third cycle. A relative error less than 5% was obtained of ν_{23C} from the remaining cycles with respect to ν_{23C} from the loading region of the first cycle when no significant plastic strains were observed. Additionally, the value of ν_{23C} obtained from the loading region of each cycle was lower than the that measured from the unloading region of the same cycle. Moreover, the latter being much larger than ν_{23C} obtained in the loading region of the first cycle.

Regarding ν^p_{23C}, plastic dilatancy was observed when the amount of compressive plastic axial strain was significantly increased ($\nu^p_{23C} > 1$ when $\varepsilon^p_{22} < -1\%$) assuming no plastic strain in the longitudinal direction ($\varepsilon^p_{11} = 0$) [13,15,16], see Fig. 12. Therefore, the analysed material behaves as a frictional material since plastic dilatancy is evidenced, i.e., volume increases due to the deviatoric plastic strain. A linear regression analysis of ν^p_{23C} vs. ε^p_{22} was performed. The intercept (1.00) of this regression analysis suggests that the analysed material presents no volumetric plastic strains ($\nu^p_{23C} \approx 1$) at small axial plastic strain assuming no plastic strain in the longitudinal direction. In addition, the coefficient of determination ($R^2 = 1.00$) and the slope (−0.05) confirm that the plastic transverse Poisson's ratio (ν^p_{23C}) linearly increases when the amount of the compressive plastic axial strain (ε^p_{22}) increases, see Fig. 12.

Table 2 summarises the transverse Poisson's ratios obtained from the corresponding linear regression analysis of the corresponding $\bar{\varepsilon}^{DIC}_{33}$ vs. $\bar{\varepsilon}^{DIC}_{22}$ curve. The comparison of ν_{23C} with ν_{23T} shows that $\nu_{23C} > \nu_{23T}$, which indicates different behaviour depending on the loading direction (compression or tension). In the elastic region, a higher expansion was observed in compression than contraction in tension, which is in agreement with the results reported by Khaled et al. [17]. In addition, the values of the elastic transverse Poisson's ratios (ν_{23C} and ν_{23T}) are similar to those reported in literature for carbon FRPs [17].

All the studied Poisson's ratios (ν_{23T}, ν_{23C} and ν^p_{23C}) in Table 2 are greater than the longitudinal Poisson's ratio ($\nu_{12} = 0.34$) in the ranges of the corresponding analysed axial strain. The same observation was found when the transverse Poisson's ratios were obtained using Eq. (2) or Eq. (3) (Figs. 8 and 10). As expected, the contraction in tension is lower in the longitudinal direction than that obtained in the transverse direction ($\nu_{12} < \nu_{23T}$), due to the stiffness of the fibres.

Lempriere [43] established the thermodynamically admissible conditions for transversally isotropic materials. The conditions prevent negative energy when the material is loaded. The rules were defined as a function of the elastic material properties. The elastic transverse Poisson's ratios reported in this work met these thermodynamic requirements of positive strain energy.

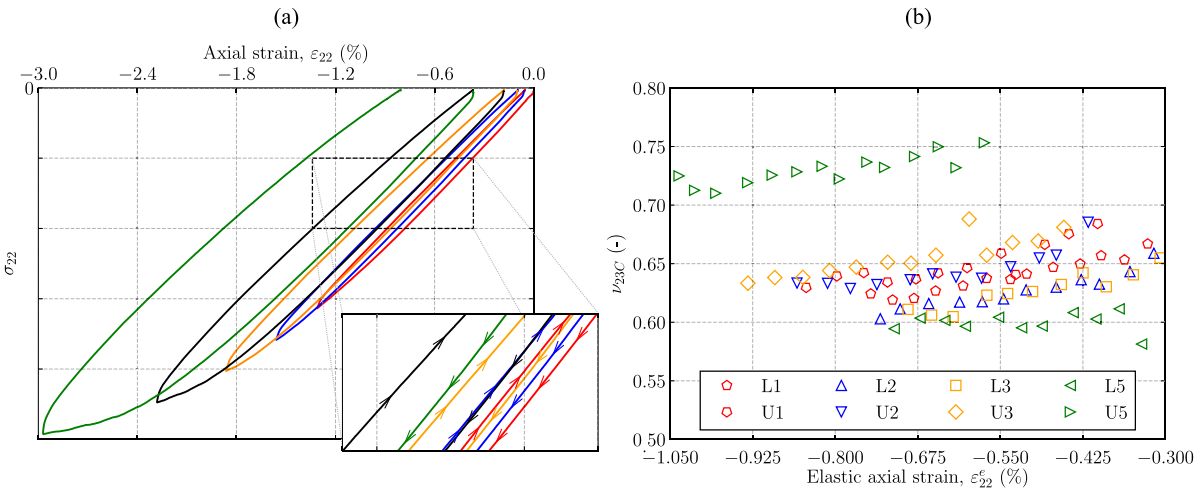

Fig. 11. Stress vs. strain curve from the transverse compressive test (a) and elastic transverse Poisson's ratio in compression vs. DIC elastic axial strain from different loading cycles (b). The results presented correspond to values from a single specimen, and *L* refers to loading region, *U* refers to unloading region and the number to the cycle.

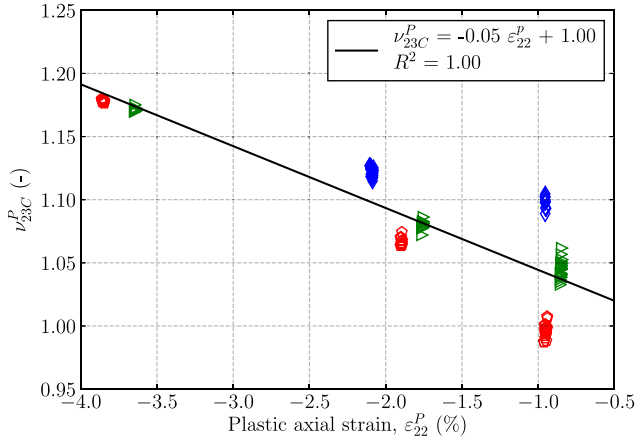

Fig. 12. Plastic transverse Poisson's ratio in compression vs. DIC plastic axial strain measured from the transverse compressive test, the different marks represents different specimens. The error bars are omitted since no significant error was measured.

Table 2
Transverse Poisson's ratio obtained from the corresponding linear regression analysis of $\bar{\varepsilon}^{DIC}_{33}$ vs. $\bar{\varepsilon}^{DIC}_{22}$, the different rows represent different specimens.

ν_{23T} (–)	ν_{23C} (–)	ν^p_{23C} (–)
0.39	0.61	1.16
0.44	0.63	1.15
0.46	0.66	1.12

4. Conclusions

A new methodology to measure the transverse Poisson's ratios for characterising a unidirectional fibre-reinforced polymer composite material at room temperature under quasi-static loading conditions has been presented. A thermoplastic-based composite material (carbon fibre/poly-ether-ether-ketone) was used to illustrate how the developed procedure was employed to measure the elastic transverse Poisson's ratios in tension and compression, as well as the plastic transverse Poisson's ratio in compression. Transverse tensile and transverse compressive tests were carried out using digital image correlation (DIC) equipment to measure the strain field on the lateral surface of the specimens. The average axial strain obtained from the DIC was compared with the one measured from two strain gauges and good agreement was found. Accordingly, the corresponding transverse Poisson's ratio was calculated from the DIC measurements.

The novelty of the present methodology, compared to those proposed in the literature, lies in the use of standard tests with additional measuring equipment and a novel data reduction method to obtain the transverse Poisson's ratio. The present method does not increase the overall number of experimental tests required for characterising a fibre-reinforced polymer composite material. Furthermore, there is no requirement for additional specimens or fixture tools.

There is a clear trend of the elastic transverse Poisson's ratio in tension to decrease when the elastic axial strain increases in two of the three specimens tested. Additionally, the elastic transverse Poisson's ratio in compression decreases when the amount of the compressive elastic axial strain increases. The comparison of the elastic transverse Poisson's ratios suggests more contraction in compression than expansion in tension. Assuming no plastic strain in the longitudinal direction, the plastic transverse Poisson's ratio in compression indicates no volumetric plastic strains for small axial plastic strains, whereas plastic dilatancy was observed as the amount of compressive plastic axial strain increased.

CRediT authorship contribution statement

I.R. Cózar: Conceptualization, Methodology, Software, Validation, Formal analysis, Investigation, Data curation, Writing – original draft. **J.J. Arbeláez-Toro:** Methodology, Software, Validation, Formal analysis, Investigation, Writing – review & editing. **P. Maimí:** Conceptualization, Methodology, Validation, Formal analysis, Supervision, Project administration, Writing – review & editing. **F. Otero:** Conceptualization, Methodology, Validation, Formal analysis, Supervision, Project administration, Writing – review & editing. **E.V. González:** Conceptualization, Methodology, Validation, Formal analysis, Supervision, Project administration, Writing – review & editing. **A. Turon:** Project administration, Funding acquisition. **P.P. Camanho:** Project administration, Funding acquisition.

Declaration of competing interest

The authors declare the following financial interests/personal relationships which may be considered as potential competing interests: Albert Turon and Emilio Gonzalez reports financial support was provided by European Commission. Pere Maimi reports financial support was provided by Spain Ministry of Science and Innovation. Ivan Cózar reports financial support was provided by Agència de gestió d'ajuts universitaris i de recerca, govern de Catalunya.

Data availability

The authors do not have permission to share data.

Acknowledgements

The first author would like to acknowledge the support of the Catalan Government (Agència de Gestió d'Ajuts Universitaris i de Recerca) through Grant 2019FI_B_01117. This work has received funding from the Clean Sky 2 Joint Undertaking (JU) under grant agreement No. 864723. The JU receives support from the European Union's Horizon 2020 research and innovation programme and the Clean Sky 2 JU members other than the European Union. This work also has been partially funded by the Spanish Government (Ministerio de Ciencia e Innovación) under contracts PID2021-126989OB-I00. Open Access funding provided thanks to the CRUE-CSIC, Spain agreement with Elsevier.

References

[1] Wang C, Liu Z, Xia B, Duan S, Nie X, Zhuang Z. Development of a new constitutive model considering the shearing effect for anisotropic progressive damage in fiber-reinforced composites. Composites B 2015;75:288–97.
[2] Zhang C, Li N, Wang W, Binienda WK, Fang H. Progressive damage simulation of triaxially braided composite using a 3D meso-scale finite element model. Compos Struct 2015;125:104–16.
[3] Tullu A, Kang B-S. Elastic deformation of fiber-reinforced multi-layered composite cylindrical shells of variable stiffness. Composites B 2016;100:44–55.
[4] Chakrapani SK, Barnard DJ, Dayal V. Nonlinear forced vibration of carbon fiber/epoxy prepreg composite beams: Theory and experiment. Composites B 2016;91:513–21.
[5] ASTM. Standard test method for tensile properties of polymer matrix composite materials (ASTM D3039/D3039M-17). West Conshohocken, PA: ASTM International; 2018, URL: www.astm.org.
[6] ASTM. Standard test method for compressive properties of polymer matrix composite materials using a combined loading compression (CLC) test fixture (ASTM D6641/D6641M-16). West Conshohocken, PA: ASTM International; 2017, URL: www.astm.org.
[7] ASTM. Standard test method for in-plane shear response of polymer matrix composite materials by tensile test of a ±45° laminate (ASTM D3518 / D3518M-18). West Conshohocken, PA: ASTM International; 2018, p. 1991, URL: www.astm.org.
[8] ASTM. Standard test method for shear properties of composite materials by the v-notched beam method (ASTM 5379/D5379M-19). West Conshohocken, PA: ASTM International; 2019, URL: www.astm.org.
[9] ASTM. Standard test method for shear properties of composite materials by v-notched rail shear method (ASTM D7078/D7078M-20). West Conshohocken, PA: ASTM International; 2020, URL: www.astm.org.
[10] Sun C-T, Rui Y. Orthotropic elasto-plastic behavior of AS4/PEEK thermoplastic composite in compression. Mech Mater 1990;10(1–2):117–25.
[11] Vieille B, Albouy W, Chevalier L, Taleb L. About the influence of stamping on thermoplastic-based composites for aeronautical applications. Composites B 2013;45(1):821–34.
[12] Vyas G, Pinho S, Robinson P. Constitutive modelling of fibre-reinforced composites with unidirectional plies using a plasticity-based approach. Compos Sci Technol 2011;71(8):1068–74.
[13] Vogler M, Rolfes R, Camanho P. Modeling the inelastic deformation and fracture of polymer composites–Part I: plasticity model. Mech Mater 2013;59:50–64.
[14] Dean A, Sahraee S, Reinoso J, Rolfes R. A new invariant-based thermo-plastic model for finite deformation analysis of short fibre reinforced composites: Development and numerical aspects. Composites B 2017;125:241–58.
[15] Cózar I, Otero F, Maimí P, González E, Miot S, Turon A, Camanho PP. A three-dimensional plastic-damage model for polymer composite materials. Composites A 2022;163:107198.
[16] Cózar I, Otero F, Maimí P, González E, Turon A, Camanho P. An enhanced constitutive model to predict plastic deformation and multiple failure mechanisms in fibre-reinforced polymer composite materials. Compos Struct 2024;330:117696.
[17] Khaled B, Shyamsunder L, Hoffarth C, Rajan SD, Goldberg RK, Carney KS, DuBois P, Blankenhorn G. Experimental characterization of composites to support an orthotropic plasticity material model. J Compos Mater 2018;52(14):1847–72.
[18] Baran I, Cinar K, Ersoy N, Akkerman R, Hattel JH. A review on the mechanical modeling of composite manufacturing processes. Arch Comput Methods Eng 2017;24:365–95.
[19] Struzziero G, Teuwen JJ, Skordos AA. Numerical optimisation of thermoset composites manufacturing processes: A review. Composites A 2019;124:105499.
[20] Gao Y, Wang J, Song X, Ding H, Wang H, Bi Y, Ke Y. Investigation on the compressive mechanical properties of ultra-thick CFRP laminates. Int J Mech Sci 2023;241:107966.
[21] Frederiksen PS. Experimental procedure and results for the identification of elastic constants of thick orthotropic plates. J Compos Mater 1997;31(4):360–82.
[22] Reddy JN. A simple higher-order theory for laminated composite plates. 1984.
[23] Kohlhauser C, Hellmich C. Determination of Poisson's ratios in isotropic, transversely isotropic, and orthotropic materials by means of combined ultrasonic-mechanical testing of normal stiffnesses: application to metals and wood. Eur J Mech A Solids 2012;33:82–98.
[24] Cui R, di Scalea FL. On the identification of the elastic properties of composites by ultrasonic guided waves and optimization algorithm. Compos Struct 2019;223:110969.
[25] De Baere I, Van Paepegem W, Degrieck J. On the nonlinear evolution of the Poisson's ratio under quasi-static loading for a carbon fabric-reinforced thermoplastic. Part I: Influence of the transverse strain sensor. Polym Test 2009;28(2):196–203.
[26] Yilmaz C, Akalin C, Kocaman ES, Suleman A, Yildiz M. Monitoring Poisson's ratio of glass fiber reinforced composites as damage index using biaxial Fiber Bragg grating sensors. Polym Test 2016;53:98–107.
[27] Trias D, Costa J, Mayugo J, Hurtado J. Random models versus periodic models for fibre reinforced composites. Comput Mater Sci 2006;38(2):316–24.
[28] Melro A, Camanho P, Pinho S. Generation of random distribution of fibres in long-fibre reinforced composites. Compos Sci Technol 2008;68(9):2092–102.
[29] Melro A, Camanho P, Pinho S. Influence of geometrical parameters on the elastic response of unidirectional composite materials. Compos Struct 2012;94(11):3223–31.
[30] Raju B, Hiremath S, Mahapatra DR. A review of micromechanics based models for effective elastic properties of reinforced polymer matrix composites. Compos Struct 2018;204:607–19.
[31] Seon G, Makeev A, Schaefer JD, Justusson B. Measurement of interlaminar tensile strength and elastic properties of composites using open-hole compression testing and digital image correlation. Appl Sci 2019;9(13):2647.
[32] Cho J, Fenner J, Werner B, Daniel I. A constitutive model for fiber-reinforced polymer composites. J Compos Mater 2010;44(26):3133–50.
[33] González E, Maimí P, Camanho P, Turon A, Mayugo J. Simulation of drop-weight impact and compression after impact tests on composite laminates. Compos Struct 2012;94(11):3364–78.
[34] Brunbauer J, Gaier C, Pinter G. Computational fatigue life prediction of continuously fibre reinforced multiaxial composites. Composites B 2015;80:269–77.
[35] Bigger R, Blaysat B, Boo C, Grewer M, Hu J, Jones A, Klein M, Raghavan K, Reu P, Schmidt T, et al. A good practices guide for digital image correlation. Int Digit Image Correl Soc 2018;94.
[36] Solutions C. Vic-2D 2010, testing guide. Technical report, Columbia: Correlated Solutions; 2010.
[37] Hoffmann K. An introduction to stress analysis and transducer design using strain gauges. In: The definitive work on strain gauge measurement. 2012.
[38] Haddadi H, Belhabib S. Use of rigid-body motion for the investigation and estimation of the measurement errors related to digital image correlation technique. Opt Lasers Eng 2008;46(2):185–96.
[39] Pan B, Qian K, Xie H, Asundi A. Two-dimensional digital image correlation for in-plane displacement and strain measurement: a review. Meas Sci Technol 2009;20(6):062001.
[40] Su Y, Zhang Q, Xu X, Gao Z. Quality assessment of speckle patterns for DIC by consideration of both systematic errors and random errors. Opt Lasers Eng 2016;86:132–42.
[41] Holmes J, Hafiz Y, Stachurski Z, Das R, Kalyanasundaram S. Surface topography evolution of woven thermoplastic composites under deformation. Composites B 2020;188:107880.
[42] Holmes J, Das R, Stachurski Z, Compston P, Kalyanasundaram S. Development of an S-specimen geometry for shear testing of woven thermoplastic composites. Composites B 2020;203:108485.
[43] Lempriere B. Poisson's ratio in orthotropic materials. AIAA J 1968;6(11):2226–7.